Radiation source displacement measurement based on spatial resolution characteristics of active pixel sensors*

Shou.Long Xu,[1] Yu.Bo Wang,[1] Qin.Xing Li,[1] Zhi.Ling Wang,[1] Zhi.Xiong Hou,[1] Cui-Yue Wei,[1] and Yi-Jun Zhong[1,†]

[1] *University of South China, Hengyang, Hunan 421001, China*

~~In this paper, we leverage the high spatial resolution and strong sensitivity to charged particles of CMOS sensors by employing the weighted centroid method to determine the displacement direction and position of radiation sources, and we evaluate its effectiveness in locating moving radiation sources. Additionally, we investigated the morphological characteristics of α-particle response signals and analyzed the response uniformity and sensitivity of different sensor regions under the influence of a collimating structure. The results indicate that the α-particle response signal is characterized by a concentration of high pixel value pixels, with 38 pixels having pixel values between 150 and 255. The sensor regions demonstrated highly consistent responses during irradiation, indicating high sensitivity to changes in the radiation source position. The peak non-uniformity value in the irradiated central region did not exceed 0.125, the non-uniformity difference between regions at the same distance was less than 0.025, and the non-uniformity of each region gradually decreased with increasing distance from the irradiated center. Compared to the classical centroid localization method, the weighted centroid method significantly improved localization accuracy and stability. Localization error gradually converged as the number of accumulated frames increased, reaching approximately 8 pixels when the number of accumulated frames reached 100. Furthermore, when tracking the continuously moving radiation source, the predicted path closely matched the actual path, with the error in the predicted centroid displacement speed being less than 5% compared to the actual speed.~~ This paper proposes a non-contact, highly sensitive detection method based on the characteristics of CMOS sensors and the weighted centroid algorithm. By conducting an in-depth study of the signal characteristics in response to α particles, the method achieves high-precision extraction of signals in the image. Additionally, a quantification model for the uniformity of sensor region responses under a collimated structure is constructed, which validates the response uniformity of the CMOS sensor. Compared to traditional centroid localization methods, the proposed algorithm improves the positioning accuracy and stability by 42.97% and 48.89%, respectively. For static source localization, the error decreases from 0.072 mm to 0.018 mm, with the error gradually converging as the accumulated frame count increases. For a continuously moving radiation source, the predicted path closely matches the actual path, and the prediction error of the displacement speed of the moving source is less than 5%. Under low frame-count conditions, the response time is less than 1 second. This method provides an effective solution for non-contact detection of sub-millimeter micro-deformations, significantly reducing the cost of surface contamination detectors for nuclear facilities, and driving innovative applications of CMOS sensors and ^{241}Am in industrial non-destructive testing and radiation monitoring.

Keywords: CMOS sensor, radiation source localization, weighted centroid method, real-time dynamic tracking

INTRODUCTION

As an important branch of nuclear radiation detection [1], ~~the localization and displacement measurement methods of α radioactive sources hold significant application value in areas such as surface nuclear radiation contamination detection [2, 3], industrial non-destructive testing [4, 5], targeted radiotherapy, and diagnostics [6, 7]. Currently, instruments used for α particle detection primarily include gas ionization detectors [8, 9], scintillation detectors [10, 11], solid-state track detectors [12, 13], time projection chambers [14, 15], and drift chambers [16]. Traditional detection methods often suffer from large equipment size, complex operation, and limited measurement accuracy [17]. Additionally, they lack digital and intelligent capabilities, making existing technologies insufficient to meet the demands of modern scientific research and industrial production. Therefore, the development of chip-level detection methods, technologies, and equipment with digital and intelligent capabilities has become a key direction in the advancement of α particle detection technology.As an efficient photosensitive element, CMOS Active Pixel Sensors (APS) can directly output digital signals and integrate multiple functions such as signal detection, processing, and readout. Leveraging their unique pixel-level signal processing capabilities, CMOS APS have achieved high-resolution, low-noise, and high-frame-rate radiation imaging [18, 29], paving new technological pathways for nuclear radiation detection. This advanced detection method not only enables high-precision and high-sensitivity detection of α particles but also offers significant advantages of compact size, low power consumption, and ease of integration [20, 21]. Currently, CMOS APS are widely used for the detection of charged particles such as γ rays [22–24], X-rays [25–27], protons [28], and low-energy electrons [29].~~

The detection and localization of α particles presents unique challenges. α particles differ significantly from other radiation particles, such as γ rays and X-rays, in terms of detection requirements. α particles have a short penetration depth and a strong ionizing ability, which requires the sensor

* National Natural Science Foundation of China (11905102).

† Yi-Jun Zhong, zhongyijun152@126.com

to have high sensitivity and high spatial resolution to accurately capture their faint signals [2]. In contrast, γ rays and X-ray detection technologies typically rely on energy measurements and radiation dose estimation, without requiring the high-resolution sensors needed for α particle detection [3, 4]. Therefore, improving the localization accuracy of α particles has become a key focus in current technological development.

Current α particle detectors mainly include gas ionization detectors [5, 6], scintillator detectors [6, 7], solid-state track detectors [8, 9], time projection chambers [10, 11], and drift chambers [12]. Traditional detection methods generally suffer from issues such as large device size, complex operation, and limited measurement accuracy [13], and also lack digital and intelligent capabilities. Existing technologies can no longer meet the needs of modern scientific research and industrial production. Therefore, the development of chip-level detection methods, technologies, and devices with digital and intelligent capabilities has become a key direction for the development of α particle detection technology. CMOS pixel sensors work by treating each pixel as an independent detection unit, with each pixel directly outputting a digital signal. CMOS APS responds to radiation events through the photoelectric or ionization effects. When α particles irradiate the pixel array of the sensor, they interact with the sensor material and generate charge. These charges are collected and processed by the space charge region within the pixel, forming a response signal related to the radiation source [14].

Compared to traditional solid-state track detectors such as the Timepix detector, diamond detectors , Medipix3 detectors[15, 16], which commonly have a pixel size of $55,\mu$m $\times$ $55,\mu$m and a pixel array size of 256×256 pixels, CMOS sensors have smaller pixels ($2.2,\mu$m $\times$ $2.2,\mu$m) and a larger pixel array size of 2592×1944 pixels. Although CMOS sensors are limited by their low-resistivity silicon-sensitive unit technology, which results in somewhat weaker radiation resistance [17], they are capable of high-precision radiation source detection in low-dose conditions due to their large pixel array and smaller pixel size. Additionally, CMOS sensors are much cheaper than other solid-state track detectors, which significantly reduces the cost of using detectors in industrial applications. They also have the significant advantages of being small in size, low in power consumption, and easily integrable [18], making large-scale deployment feasible. Currently, CMOS APS is widely used in ionizing radiation detection fields such as γ rays [19–21], X-rays [22–24], protons [25], and low-energy electrons [26].

~~hile researchers in the field have begun exploring new methods for radiation source localization, there is a scarcity of research reports specifically on α radioactive source localization. Studying the localization methods of α radioactive sources using CMOS APS will contribute to enhancing the accuracy and efficiency of nuclear safety monitoring, environmental protection, and medical diagnostics.~~ Although researchers in this field have begun to explore new methods for radiation source localization, research reports on the localization of α radiation sources are still relatively scarce. Research on CMOS APS-based α radiation source localization methods will help improve the accuracy and efficiency of nuclear safety monitoring, industrial non-destructive testing, and medical diagnostics. Research has shown that CMOS sensors can maintain uniform temporal and spatial response and sensitivity under stable radiation fields [27–29]. However, most studies have focused on the gamma radiation field, with few reports on sensor uniformity and response variations induced by α radioactive sources. In the field of radiation source localization and displacement measurement, the industry primarily employs the following methods: geometric localization, spectral analysis, machine learning and deep learning algorithms, and image processing techniques. Geometric localization involves deploying multiple detectors to measure the distances or angles between the radiation source and each detector, using triangulation principles to determine the source's position. This method can achieve high-precision source localization under reasonable detector arrangement and favorable environmental conditions, but the simultaneous use of multiple detectors increases system complexity and cost [30–32]. Spectral analysis determines the position of the radiation source by utilizing the unique energy spectra emitted by the source in conjunction with energy information and spatial distribution characteristics. This allows for precise localization using the distinctive spectral features of the source but requires high-precision energy measurement equipment and is only applicable when the source has clearly defined spectral characteristics [33–35]. Machine learning and deep learning methods can handle diverse and complex radiation detection data and have good generalization capabilities; however, they require large amounts of labeled data for training, making data collection and labeling time-consuming and costly [36, 37]. Image processing methods, such as those using Compton cameras and scintillation detectors, utilize scattering events and optical imaging techniques to accurately determine the position of the radiation source. However, the complex structure and high manufacturing cost of Compton cameras limit their widespread application, and the resolution of scintillator materials and optical systems restrict imaging precision, making it difficult to meet the demands for high-precision localization [38, 39]. In summary, although current methods can address radiation source localization and displacement measurement to some extent, they are limited in achieving fine displacement measurements and directional determination of radiation sources.

~~This paper proposes a novel method for determining and measuring the displacement of radiation sources. Through radiation response experiments, the overall response capability of the CMOS APS pixel array was investigated. Based on the morphological characteristics of radiation response events and the distribution characteristics of response signals under the influence of collimating structures, a density-based clustering algorithm was introduced. A method for determining and measuring the displacement of radiation sources was proposed, and the localization of radiation sources, determination of displacement direction, and measurement accuracy were experimentally validated. The research findings presented in this paper not only~~

~~provide new methods and technologies for radiation source localization and non-contact displacement measurement but also expand the application market for ^{241}Am isotope radiation sources.~~ This paper proposes a new method for determining and measuring radiation source displacement. By conducting radiation response experiments, the overall response capability of the CMOS APS pixel array is investigated. Based on the morphological features of radiation response events and the response signal distribution characteristics under the influence of the collimated structure, the DBSCAN density clustering algorithm [40, 41] is introduced to propose a method for determining and measuring radiation source displacement. Experimental results show that the localization accuracy for static α radiation sources can achieve micron-level precision. The displacement direction and speed of the radiation source are measured with an error of less than 5%, and the method provides a sensitive response to the displacement of α radiation sources under low frame conditions, with a response time of less than 1 second. These findings have significant potential in the development of high-precision non-destructive testing instruments at the sub-millimeter level and new non-contact surface contamination detectors.

I. EXPERIMENTAL PREPARATION

A. Experimental Samples and Conditions

~~The experiment used a SONY MT9P031 active pixel sensor, featuring a pixel size of $2.2\,\mu m \times 2.2\,\mu m$ and an effective resolution of 2592 horizontal by 1944 vertical pixels, covering an active area of 6 mm (H) $\times$ 4 mm (V). The sensor supports 810 bit digital signal output. To ensure consistent and clear response signals, the sensor gain was fixed at 50 dB and the integration time was set to 45 ms. The glass protective layer on the sensor surface was removed to allow alpha rays (α rays) to penetrate the silicon pixel array. Data acquisition and processing were performed using the iCamera 51 microcontroller, with image data transmitted from the sensor module to the PC via a high-speed USB interface at a sampling frequency of 25 Hz.~~

The experiment employed a SONY MT9P031 Active Pixel Sensor (APS) [42], featuring a pixel size of $2.2\,\mu m \times 2.2\,\mu m$ and a native resolution of 2592 (horizontal) $\times$ 1944 (vertical) pixels. The active area measures 6 mm (H) $\times$ 4 mm (V), with 8–10-bit digital signal output capability. To ensure signal response uniformity and image clarity, the sensor gain was fixed at 50 dB with an integration time of 45 ms. The protective glass cover was removed to enable direct α-particle penetration into the silicon pixel array. Data acquisition and processing were implemented through an iCamera51 microcontroller (customized device), where image data transmission to the host PC was achieved via a high-speed USB interface at 25 Hz sampling frequency.

This study used a ^{241}Am alpha radiation source with a diameter of 2.13 mm, a characteristic alpha-ray energy of 5485.56 keV and a radioactive activity of 29 kBq. In the absence of a collimating structure, the alpha particle flux rate on the sensor surface was 1.05×10^4 cm^{-2}s^{-1}. When a collimating structure was introduced, the flux rate decreased to 5.87×10^3 cm^{-2}s^{-1}. The experiments were conducted at room temperature, maintained at 25 řC.

A radiation source tracking platform was designed to facilitate the horizontal displacement of the radiation source, which was consistently positioned 5 mm above the sensor surface. A collimating structure was developed to produce a collimated and calibrated alpha-ray beam. The collimator featured a circular aperture with a diameter of 0.7 mm and a length of 1 mm. The experimental setup and test system are illustrated in Figure 1.

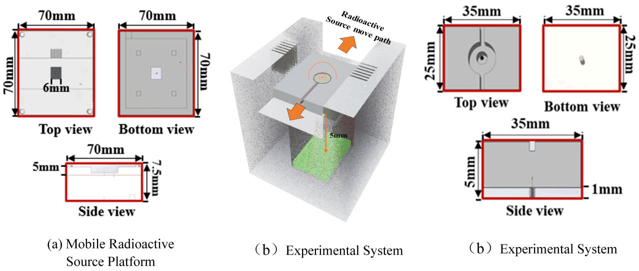

Fig. 1: Experimental System Diagram

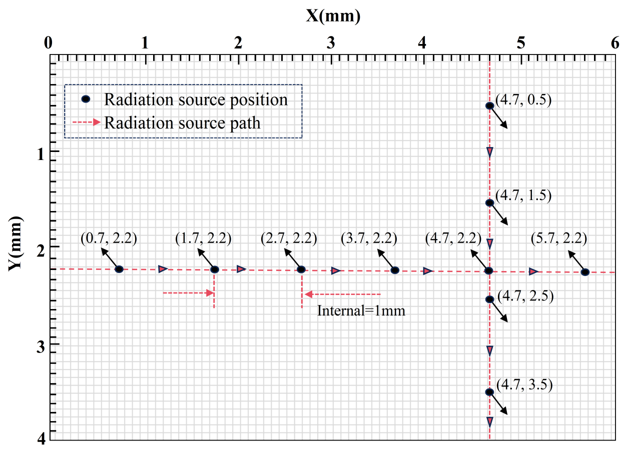

Fig. 2: Diagram of the Movement Path and Irradiation Point Selection

Table 1: Experimental Scheme

Experiment No.	Initial Coordinate/mm	Horizontal Displacement/mm	Vertical Displacement/mm
No.1	(2.7, 2.2)	0	0
No.2	(4.7, 0.5)	0	1
No.3	(0.7, 2.2)	1	0

During the experiment, the top-left position was designated as the origin. A total of 500 image frames were collected, the

radiation source displaced by a specific distance between each acquisition for statistical analysis. The experimental scheme is detailed in Table 1. Figure 2 illustrates the path of movement and the selection of irradiation points.

Table 2: Experimental Configuration for Moving Source Localization

Experiment No.	Initial Coordinate/mm	Terminal Coordinate/mm
No.1	(0, 2.5)	(6, 2.5)
No.2	(3.5, 0)	(3.5, 4)

For the displacement measurement experiment of a continuously moving radioactive source, the sensor was fixed at the coordinate origin while the radioactive source was translated at a constant velocity of 1mm/s. A total of 150 consecutive frames were acquired in each experimental trial. Upon completion of data acquisition, the moving direction and velocity of the radioactive source were analyzed in 25-frame batches. The experimental parameters are summarized in Table 2.

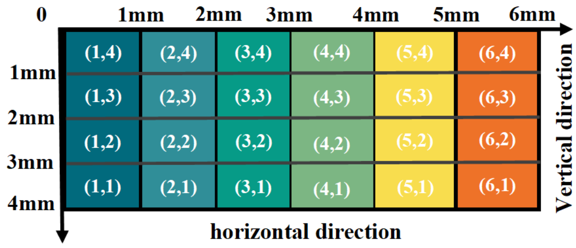

(a) Sensor Pixel Array Partitioning

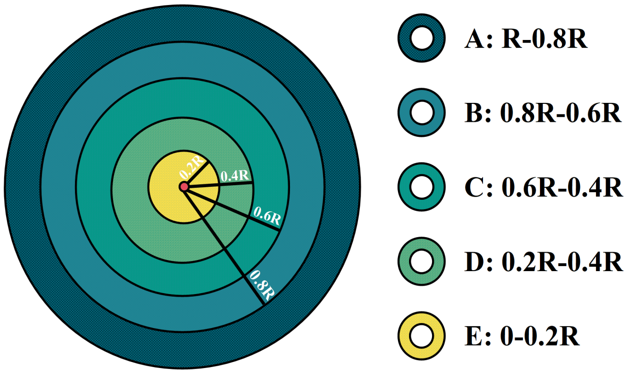

(b) Density Ring Band

Fig. 3: Pixel Array Region

B. Data Processing Methods

To calculate the rate of increase A_k of pixels within each pixel value interval and identify the interval most significantly affected by irradiation, the following formula is employed: $\cancel{A_k = \frac{P_k^a}{P_k^b}}$

$$A_k = \frac{P_k^b}{P_k^a} \tag{1}$$

where P_k^a and P_k^b represent the proportion of pixels in the k-th pixel value interval before and after irradiation, respectively.

For pixels in various pixel value intervals, the proportion P_n of pixels in the eight neighboring pixels that belong to the same interval is calculated to assess the morphological characteristics of pixel aggregation: $\cancel{P_n = \frac{S_n}{S_j}}$

$$P_n = \frac{S_j}{S_n} \tag{2}$$

where S_n is the number of target pixels surrounded by eight neighboring pixels within the same pixel value interval, and S_j is the total number of target pixels in the pixel value interval $[g_k, g_{k+1}]$.

To evaluate the uniformity of the pixel array response and the morphological characteristics under the influence of a collimating structure, the entire CMOS active pixel sensor array is divided into 24 equal regions. Additionally, the signal-concentrated area is uniformly partitioned into five annular bands, as illustrated in figure 3.

To calculate the cumulative pixel value value E_i for each region to analyze the uniformity of the sensor's response when irradiating a specific region, the following formula is used: $\cancel{E_i = \sum_{t=1}^{N} E_{ti}}$

$$E_i = \sum_{t=1}^{N} E_{ti} \tag{3}$$

where N is the total number of images, and $E_{t,i}$ is the pixel value value of region i in the t-th frame.

The non-uniformity R_{nud} of different regions in the pixel array represents the response differences between regions when the radiation source irradiates specific regions of the sensor: $\cancel{R_{nud} = \frac{1}{S_i}\sqrt{\frac{1}{h}\sum_{n=1}^{h}(v_{xni} - S_i)^2}}$

$$R_{\mathrm{nud}} = \frac{1}{S_i}\sqrt{\frac{1}{h}\sum_{n=1}^{h}(v_{xni} - S_i)^2} \tag{4}$$

where v_{xni} is the total pixel value of region i in the n-th image after moving the radiation source x mm, h is the total number of images, and S_i is the average pixel value of region i after a movement distance of x mm.

After overlaying the response signals from frames i to $i+k$

to construct a point set, annular regions are divided based on radii of $0.8d$, $0.6d$, $0.4d$, and $0.2d$, where d is the average distance from the boundary to the centroid. The signal concentration C within each band is calculated as: $\cancel{C = N_S}$

$$C = \frac{N}{S} \tag{5}$$

where N is the number of response signals in the band, and S is the area of the band.

$$\bar{d} = \frac{1}{N}\sum_{i=1}^{N} d_i = \frac{1}{N}\sum_{i=1}^{N}\sqrt{(x_{c_i} - x_r)^2 + (y_{c_i} - y_r)^2} \tag{6}$$

where N denotes the number of weighted centroid groups (equivalent to accumulated frames), (x_{c_i}, y_{c_i}) represents the i-th weighted centroid coordinates, and (x_r, y_r) indicates the ground-truth projection coordinates.

To validate the algorithm's effectiveness, we quantify localization contributions through stratified Fisher information analysis and compute the Cramér-Rao Lower Bound (CRLB) [?]under different accumulation conditions:

The observed position of the i-th response signal (x_i, y_i) and the actual position of the radiation source (x_s, y_s) are defined by the following relationship:

$$x_i = x_s + n_{xi}, \quad y_i = y_s + n_{yi} \tag{7}$$

In the above equation, (x_s, y_s) represents the actual position of the radiation source, (x_i, y_i) denotes the observed position coordinates of the i-th detected signal, n_{xi}, n_{yi} represents the random measurement error in the observed position, which can be either positive or negative.

Through experimental calibration, we measure the predicted position (x_c, y_c) and the actual position (x_s, y_s) and define the error between them. First, the squared prediction error for a single experiment is defined as:

$$e_j^2 = (x_{c,j} - x_s)^2 + (y_{c,j} - y_s)^2 \tag{8}$$

Here, $(x_{c,j}, y_{c,j})$ represents the predicted position coordinates obtained by the algorithm in the j-th experiment, (x_s, y_s) denotes the actual position of the radiation source. Then, using multiple independent experiments (a total of M experiments), the average variance of the prediction error is calculated as follows:

$$\sigma_i^2 = \frac{1}{M}\sum_{j=1}^{M} e_j^2 \tag{9}$$

Through experimental calibration, we measure the predicted position (x_c, y_c) and the actual position (x_s, y_s) and define the error between them. First, the squared prediction error for a single experiment is defined as:

$$e_j^2 = (x_{c,j} - x_s)^2 + (y_{c,j} - y_s)^2 \tag{10}$$

Here, $(x_{c,j}, y_{c,j})$ represents the predicted position coordinates obtained by the algorithm in the j-th experiment, (x_s, y_s) denotes the actual position of the radiation source. Then, using multiple independent experiments (a total of M experiments), the average variance of the prediction error is calculated as follows:

$$\sigma_i^2 = \frac{1}{M}\sum_{j=1}^{M} e_j^2 \tag{11}$$

Here, σ_i^2 represents the variance of the prediction error obtained from actual experimental observations, indicating the degree of uncertainty in measurement errors. Based on the clearly defined measurement error variance, we strictly assume that the measurement errors for each observed signal position follow an independent and identically distributed Gaussian distribution:

$$n_{xi}, n_{yi} \sim N(0, \sigma_i^2) \tag{12}$$

The above equation indicates that the position error terms for the i-th response Signal, n_{xi}, n_{yi}, are random variables following a normal distribution with zero mean and variance σ_i^2. This means that the observed positions are randomly distributed around the actual position without systematic bias. Under the Gaussian error assumption, the joint likelihood function of the observed data can be expressed as:

$$L(\mathbf{x}, \mathbf{y} | x_s, y_s) = \prod_{i=1}^{N} \frac{1}{2\pi\sigma_i^2} \exp\left[\frac{-(x_i - x_s)^2 + (y_i - y_s)^2}{2\sigma_i^2}\right] \tag{13}$$

This equation provides the joint probability density expression for observing a series of signal positions, (x_s, y_s), given the actual position parameters, (x_i, y_i), where N represents the total number of observed signals. Taking the natural logarithm of the above likelihood function yields the log-likelihood function.

Taking the natural logarithm of the likelihood function, we obtain the log-likelihood function:

$$\ln L = -\sum_{i=1}^{N}\left[\ln\left(2\pi\sigma_i^2\right) + \frac{(x_i - x_s)^2 + (y_i - y_s)^2}{2\sigma_i^2}\right] \tag{14}$$

This equation represents the logarithmic form of the likelihood function, facilitating mathematical analysis and clearly illustrating the statistical characteristics of errors between observed and actual positions. Using the log-likelihood function, we define the Fisher information matrix as follows:

$$\mathbf{I}(x_s, y_s) = \begin{bmatrix} \sum_{i=1}^{N} \frac{1}{\sigma_i^2} & 0 \\ 0 & \sum_{i=1}^{N} \frac{1}{\sigma_i^2} \end{bmatrix} \tag{15}$$

The above matrix quantifies the amount of information that the observed data provides about the parameters being estimated, (x_s, y_s), thereby determining the theoretical precision of parameter estimation.

The Cramér-Rao Lower Bound (CRLB) is defined as the inverse of the Fisher information matrix, representing the best achievable theoretical accuracy for position estimation:

$$\mathbf{CRLB}(x_s, y_s) = \mathbf{I}^{-1}(x_s, y_s) = \begin{bmatrix} \frac{1}{\sum_{i=1}^{N} \frac{1}{\sigma_i^2}} & 0 \\ 0 & \frac{1}{\sum_{i=1}^{N} \frac{1}{\sigma_i^2}} \end{bmatrix} \tag{16}$$

The diagonal elements of this matrix correspond to the theoretical lower bounds of the estimation variance for position parameters, meaning that no unbiased estimator can achieve a variance lower than this theoretical limit.

To determine the constant k in the relationship between w_i and σ_i^2, the average total weight from multiple experiments is defined as follows:

$$W = \frac{1}{M} \sum_{j=1}^{M} \sum_{i=1}^{N_j} w_{i,j} \tag{17}$$

Here, $w_{i,j}$ represents the weight calculated for the i-th observation point in the j-th experiment after entropy-weighted fusion. Based on this, the constant k is determined as follows:

$$k = \sigma_i^2 \cdot W \tag{18}$$

where, σ_i^2 is the average variance of the prediction error obtained through actual measurements.

Finally, using the experimentally calibrated constant k, the theoretical lower bound of the positioning accuracy for this algorithm is explicitly computed:

$$\sigma_{ideal} = \sqrt{\frac{k}{\sum_{i=1}^{N} w_i}} \tag{19}$$

This equation clearly defines the minimum possible prediction position error achievable under the current algorithm, representing the theoretical limit of the algorithm's performance.

II. EXPERIMENTAL RESULTS AND DISCUSSION

~~Figure 4 presents three-dimensional scatter plots of the sensor's pixel value matrices before and after irradiation. In Figure 4a, the pixel value image before irradiation exhibits a relatively stable baseline formed by background noise. The pixel values are primarily distributed in the range of 0 to 50, with only a few noise peaks. This background noise mainly originates from the sensor's dark current and readout noise, which are inherent signals present when the sensor operates without external light or radiation.~~

A. Global Response Analysis of the Pixel Array

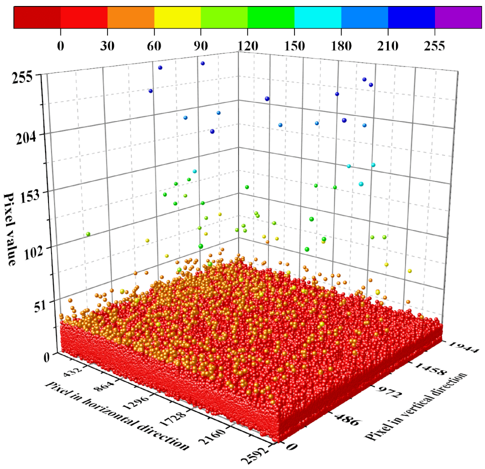

(a) Dark-field image of pixel value matrix under non-collimated source pre-irradiation

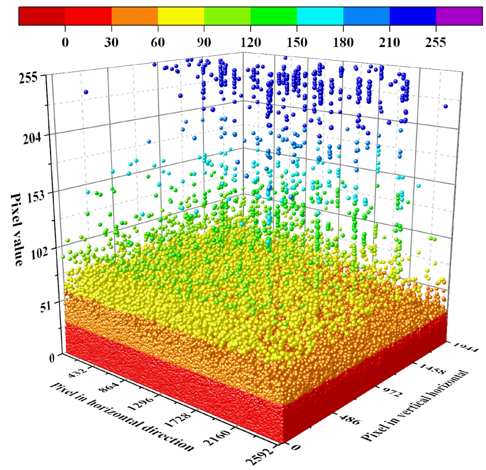

(b) Dark-field image of pixel value matrix during non-collimated irradiation

Fig. 4: Comparative 3D scatter plots of pixel value matrix pre-/during non-collimated source irradiation

Figure 4 shows the three-dimensional scatter plots of the entire sensor pixel matrix before and after irradiation with a non-collimated source. In Fig. 4a, the pre-irradiation pixel value distribution exhibits a relatively stable baseline composed of background noise. The pixel values are primarily distributed between 0 and 50, with only a few noise peaks. This background noise mainly originates from the sensor's dark current and readout noise, which are inherent signals generated when the sensor operates without external illumination or radiation.

~~In contrast, figure 4b shows the dark image during irradiation. It can be observed that many pixels exhibit significantly increased pixel values, although the number of pixels decreases as the pixel value increases. This phenomenon occurs because alpha particleshigh-energy, positively charged helium nucleiundergo strong ionizing collisions with atoms and electrons in the semiconductor material as they pass through it, rapidly depositing their energy over a very short distance.~~

These collisions generate a large number of electron-hole pairs in the semiconductor material. As alpha particles traverse the sensor, the pixels along their paths produce strong electrical signals due to the substantial generation of electron-hole pairs, leading to significant increases in their pixel values. Because alpha particles have a short range (approximately tens of micrometers in solids), their impact is primarily concentrated in localized regions.

~~Table 4 presents the proportions of pixels in different pixel value intervals for 500 frames of images before and during irradiation. According to the statistical data, the proportion of pixels in the 50100 interval increased by 34.6 times, in the 100150 interval by 19 times, in the 150200 interval by 47.3 times, and in the 200255 interval by 25.5 times.~~

Table 4 shows the proportional distribution of pixel values across different intensity ranges within a 500-frame dataset before and after irradiation. Statistical analysis reveals enhancement factors of 32.29 for the 50-100 range, 22.50 for 100-150, 46.25 for 150-200, and 34.29 for the 200-255 range.

Table 4: Distribution of pixel values

Pixel Value Range	**Before Irradiation (%)**	**During Irradiation (%)**	**Increase Factor**
50 to 100	0.96×10^{-3}	0.31×10^{-1}	32.29
101 to 150	0.36×10^{-3}	0.81×10^{-2}	22.50
151 to 200	0.16×10^{-3}	0.74×10^{-2}	46.25
201 to 255	0.21×10^{-3}	0.72×10^{-2}	34.29

~~These results indicate that the energy deposition of alpha particles during irradiation significantly affects the pixel response of the sensor. In particular, in the 150–200 pixel value interval, the increase in the proportion of pixels is the largest, reaching 47.3 times. In summary, within this energy range, the impact of alpha particles on the sensor is the most significant.~~

This phenomenon originates from the energy deposition mechanism of alpha particles interacting with the sensor. The deposited charge density exhibits radial attenuation from the interaction site, with complete dissipation beyond critical diffusion distances. Proximity to the particle-sensor interaction site correlates with enhanced pixel value elevation gradients and consequent population proportion increments.

B. Response Event Characteristics

~~Figure 5 presents the typical radiation event of the CMOS sensor exposed to the ^{241}Am α radiation source, depicted as a 3D bar chart and a heatmap. As shown in Figure 5a, the response is characterized by a sharp increase or saturation in the pixel values of multiple adjacent pixels in a specific region, while pixel value changes in other regions are relatively small. Consequently, the peak of the response event is relatively steep. This occurs because α particles deposit high energy in a specific region of the sensor, generating numerous electron-hole pairs. This leads to a rapid increase in the charge of adjacent pixels, forming a prominent pixel value peak. Meanwhile, other regions of the sensor are not directly irradiated, resulting in insignificant pixel value changes and a low noise level.~~

Figure 5 demonstrates typical radiation signals generated by a CMOS sensor exposed to a non-collimated ^{241}Am α-source, presented through 3D bar plots and heatmaps. As shown in Fig. 5a, the response characteristic manifests as a sharp increase or saturation of pixel values in localized adjacent pixels, while other regions exhibit minimal variation. Consequently, the signal peaks display steep gradients. This phenomenon occurs becauseα-particles deposit concentrated energy within specific sensor areas, generating substantial electron-hole pairs. The resultant charge accumulation rapidly elevates adjacent pixel values, forming distinct intensity peaks.

Although noise-induced variations in pixel gray values can fall within the same range as those caused by α particle events, the area affected by noise is smaller, generally involving only single pixels. This indicates that noise-induced pixel value changes are usually isolated and scattered, without forming prominent peak regions. Figure 5b shows the heatmap of pixel value distributions for α response events. During such an event, the gray values of multiple closely connected pixels significantly increase, forming concentrated areas of high gray values.

To further quantify the characteristics of α-particle response signals, we conducted comparative analyses between non-irradiated and irradiated images. In non-irradiated images: isolated pixels with intensity values exceeding 150 account for only 0.00023% of the total pixels; pixels with connectivity numbers of 1-2 and intensity values all above 150 constitute 0.00001%; red no pixel clusters with connectivity numbers of 3-8 and intensity values above 150 were observed.

In images acquired during radioactive source irradiation: the proportion of isolated pixels (>150 intensity) increased from 0.00013% to 0.00328%; pixels with connectivity 1-2 (>150 intensity) rose to 0.00204%; while clusters with

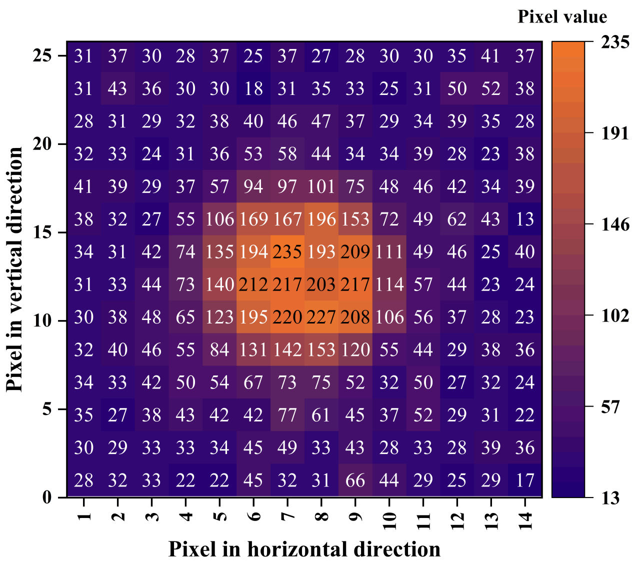

(a) Heatmap of Typical radiation events

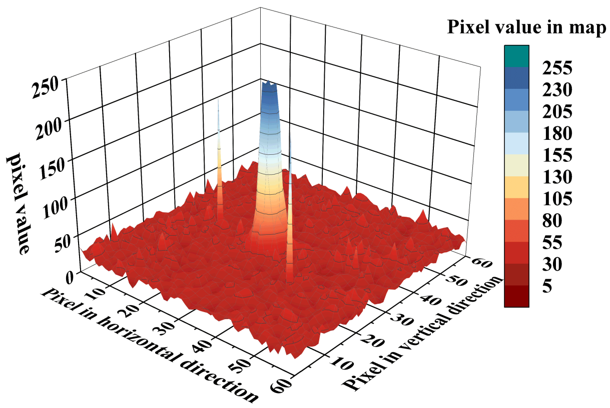

(b) Comparison between α response events and noise.

Fig. 5: Typical radiation events and the comparison between response events and noise during non-collimated irradiation

connectivity 3-8 (>150 intensity) significantly increased to 2.0570%.

Figure 6 illustrates the proportion curves of pixel clusters for different gray value intervals. Under radiation, pixels with gray values in the 50–150 range have over 90% of their neighboring pixels containing only one or two pixels with similar gray values, while cases with three or more neighboring pixels in the same range account for less than 5%. This indicates that pixel distribution in this gray value interval is relatively scattered, lacking evident clustering characteristics. This dispersiveness mainly originates from background noise and the scattering of low-energy α particles within the material, leading to slight increases in individual pixel gray values that are insufficient to form continuous high-gray-value regions.

In contrast, pixels with gray values in the 150–255 range typically have more than three neighboring pixels within the same interval, showing highly concentrated distributions of high-gray-value pixels. This clustering is due to the strong ionization effects caused by α particles interacting with the sensor material. As α particles traverse the semiconductor material, they generate numerous electron-hole pairs along their paths, significantly elevating the gray values of adjacent pixels. Due to the short range of α particles, the deposited ionization charges easily enter the space charge regions of neighboring pixels, resulting in clusters of high-gray-value pixels forming circular spots.

The reduction in the proportion of Category 6 is attributed to the energy deposition pattern of particles on the pixel sensor and the incidence angles of alpha particles. When an alpha particle interacts with the CMOS sensor, its energy diffuses radially outward from the point of contact, gradually diminishing until complete dissipation. This process creates distinct concentric banding characteristics in the grayscale values of pixels within the alpha response signalhigher values near the geometric center and a gradual decrease toward the periphery. However, due to the scattering of alpha particles, their incidence angles are not perfectly perpendicular. Consequently, when interacting with the sensor, their energy deposition exhibits directional bias, resulting in disparities in charge intensity distribution across different orientations. This directional asymmetry in charge generation and diffusion directly contributes to the observed decline in Category 6 prevalence.

Based on these characteristics, we utilize the spatial clustering property of high-gray-value pixels to identify and extract α particle response signals using a connected region algorithm. Specifically, pixels with gray values in the 150–255 range are selected as samples. The connected regions are constrained to contain between three and eight pixels to ensure that the extracted regions result from high-energy deposition by α particles rather than random noise or other factors. This approach enables the effective and high-precision extraction of α particle response signals from the image.

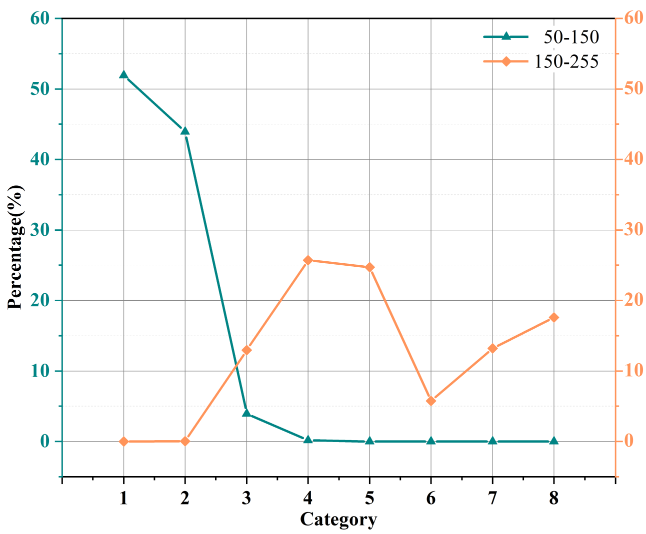

Fig. 6: Pixel Cluster Distribution

C. Analysis of the Response Signal Distribution Characteristics Under Collimating Structure Interference

~~Figure 7 illustrates the maximum ring radius of the response signal distribution area as a function of the number of accumulated frames under the influence of the collimating structure. The figure demonstrates that the maximum radius increases with the number of accumulated frames, although the rate of growth gradually decreases. Specifically, between 15 and 40 accumulated frames, the radius increases rapidly. Beyond 40 frames, the growth rate significantly slows, with the radius expanding from 720 to 740 units as the number of frames increases from 40 to 100. From 100 to 160 frames, the radius growth nearly halts.~~

Figure 7 demonstrates the variation of the maximum annular radius in response signal distribution regions under collimator structure influence as a function of accumulated frames. The results indicate that the maximum radius increases with frame accumulation but exhibits progressively decelerating growth. Specifically: From 15 to 40 frames, the radius rapidly expands from 1.55 mm to 1.65 mm; beyond 40 frames, the growth rate substantially decreases, reaching 1.69 units when frames increase from 40 to 100; from 100 to 160 frames, the radius growth nearly plateaus.

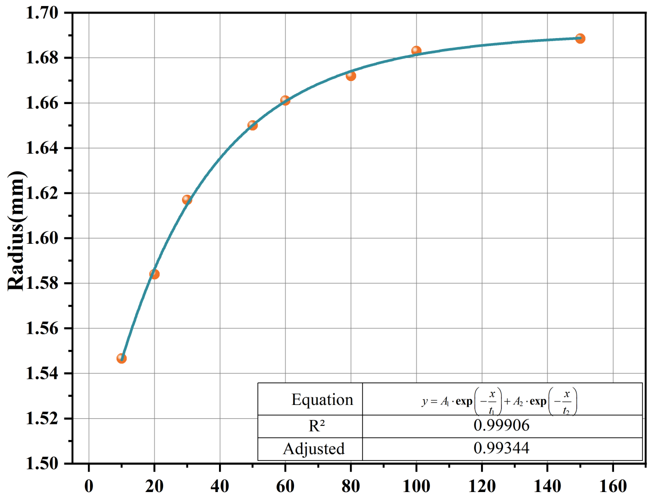

Fig. 7: Relationship between Frame Count and Radius

This trend indicates that, initially, the accumulation of α particle response events leads to concentrated radiation energy deposition on the sensor, resulting in a rapid increase in the radius. This rapid initial growth reflects the sensor's high sensitivity to the initial radiation energy. As the number of accumulated frames increases, the system gradually approaches saturation, and the cumulative effect of response events diminishes, slowing the radius growth. This suggests that most active regions have been detected, and new response events contribute less to the radius. In the later stages, the system reaches a nearly balanced state, with minimal increases in α particle response events, resulting in almost no further growth in the radius.

This phenomenon can be attributed to two factors. First, α particles scatter, and due to spatial angular effects, response signals from particles at the outer edges of one side of the detector originate from particles at the outermost edge on the opposite side of the radiation source. The longer travel distance and greater energy loss in the air result in fewer signals, leading to significantly fewer response signals at the outermost edges compared to the central region. Consequently, this phenomenon is not apparent when the number of frames is low but becomes more pronounced as the number of accumulated frames increases, causing the radius to grow. Therefore, under the influence of a collimating structure, the radius of the concentrated response event region can be considered constant.

~~Figure 8 illustrates the frame images of response events and the density distribution curves in the ring band region of figure 8b for different numbers of accumulated frames. As shown, the density variation of each ring band follows a consistent pattern: the density of response events increases as the distance from the center decreases. In the circular region with a radius of $0.2R$, the response event density reaches its maximum value. In the ring band between $0.2R$ and $0.4R$, although the density decreases, it remains relatively high. Over 40% of the response signals are concentrated within the circular region of radius $0.4R$, which accounts for only 16% of the total area. This indicates that, under the interference of the collimating structure, the radiation energy from the source is most concentrated in the central region, resulting in the highest density of response events near the center. This concentration occurs because α particles have limited penetration ability but strong ionization capability, causing most of their energy to be deposited in the central region. Additionally, the geometric concentration effect ensures that the central region occupies a symmetrical and concentrated spatial position, and the radiation energy propagates in a geometrically symmetrical manner, further enhancing the radiation density in the central region.~~

Figure 8 presents the frame images of response events at different cumulative frame counts and the density distribution curves of signals within the annular regions. The specific division method of the annular regions is shown in Figure 3a. We extracted and superimposed all the response signals in the image, calculated the centroid coordinates based on all response signals, and determined the distance R from the centroid to the farthest signal. Using $0.8R$, $0.6R$, $0.4R$, and $0.2R$ as radii, circular regions were drawn to define different annular regions, and the density of response signals in these regions was calculated. Figure 8a illustrates the schematic diagram of response signal distribution within different annular regions under varying cumulative frame counts, while Figure 8b presents the density distribution curves of the annular regions.

As shown in the figure, the density variation within each annular region follows a consistent pattern: the density of response events increases as the distance to the center decreases. Within the circular region of radius $0.2R$, the response event density reaches its maximum. In the annular region between $0.2R$ and $0.4R$, although the density decreases, it remains at a relatively high level. More than 40% of the re-

sponse signals are concentrated within the circular region of radius $0.4R$, despite this region accounting for only 16% of the total area. This indicates that under the interference of the collimator structure, the radiation energy of the source is most concentrated in the central region, resulting in the highest density of response events near the center. This concentration phenomenon occurs because particles have a limited penetration ability, but their strong ionization capability causes most of their energy to be deposited in the central region. Additionally, the geometric focusing effect ensures that the central region occupies a symmetric and concentrated spatial position, where radiation energy propagates in a geometrically symmetric manner, further enhancing the radiation density in the central region.

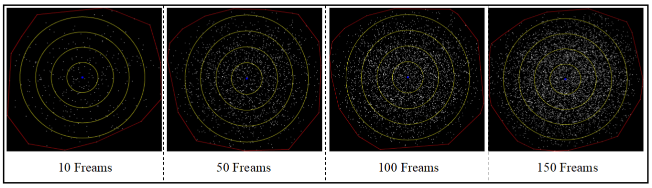

(a) Schematic of Signal Distribution Characteristics in Annular Regions under Multi-Frame Superposition Conditions

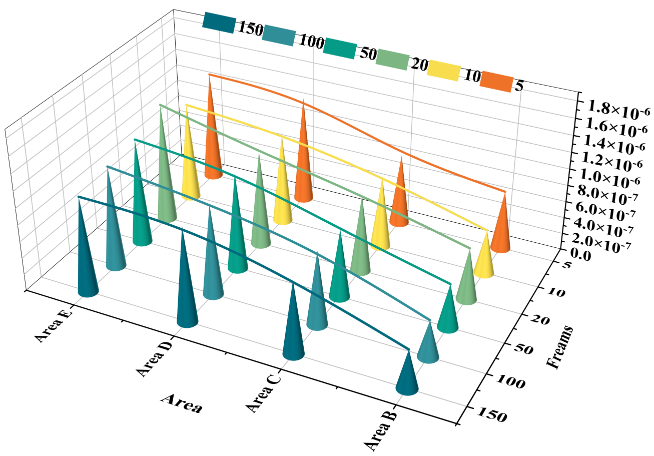

(b) Analytical Map of Signal Density Correlation in Annular Bands with Frame Count Evolution

Fig. 8: Spatial Distribution Characterization of Signal Density in Annular Zones Calibrated by Collimated Source

~~Figure 9 illustrates the variation of accumulated pixel values in different regions when the radiation source, positioned as shown in Figure 3a, irradiates the sensor under the influence of the collimation structure.~~

Figure 9 demonstrates the variation of cumulative pixel intensity values across distinct regions of the monolithic sensor's pixel array when the radiation source is positioned as schematically depicted in Figure 3a, and irradiates the detector under the collimation-induced spatial modulation.

As depicted in the figure, the irradiated regions exhibit a consistent response trend: as the number of accumulated frames increases, the accumulated pixel values in each region increase linearly, and the peak values across different regions are very similar. The linear increase in pixel values after stacking frames reflects the sensor's stable response to continuously incident particles. In each frame, the number of particles and the energy deposition experienced by the sensor pixels remain constant, leading to the same pixel value increment per frame. This linear relationship indicates that the sensor's response to particle incidence is linear, meaning the output signal strength is directly proportional to the number of incident particles and their energy. Meanwhile, the similarity of peak values across regions demonstrates the spatial uniformity of the sensor's response. This implies that different regions of the sensor have similar response efficiencies under identical irradiation conditions. Therefore, separate calibration or compensation for different regions of the sensor is unnecessary. Thus, displacing the radiation source to different positions will produce consistent signal variations.

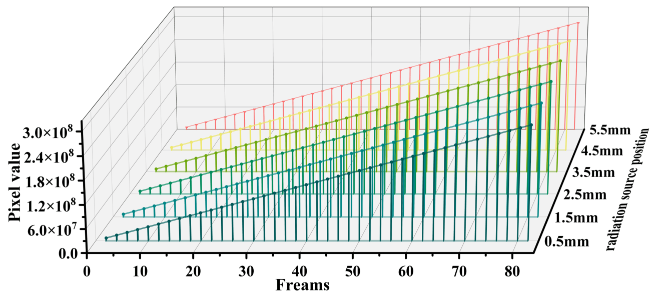

Fig. 9: The cumulative pixel values of the corresponding regions under different irradiation positions

~~Figure 10 illustrates the nonuniformity distribution across different regions of the CMOS sensor when the radiation source is positioned at various irradiation points with the collimation structure in place. As depicted, when the radiation source directly irradiates a specific region of the sensor, the nonuniformity in that region reaches its maximum value. Although this maximum does not exceed 0.125, it is significantly higher than that in other regions.~~

~~The maximum difference in nonuniformity peak values between regions is less than 0.025, reflecting the overall consistency of the sensor's response.As the distance from the irradiated center increases, the nonuniformity in the regions gradually decreases. This trend occurs because the particle flux density decreases with increasing distance due to spatial diffusion and scattering effects. As particles propagate through the medium, they lose energy and change direction, leading to reduced energy deposition in regions farther from the center. This spatial distribution of energy deposition results in decreased nonuniformity.Moreover, this trend indicates that as the position of the radiation source changes, the energy deposition distribution in the irradiated region also changes, leading to variations in the nonuniformity distribution. The sensor can sensitively detect the movement of the radiation source by monitoring these changes. This demonstrates that under steady-state radiation field conditions, the CMOS sensor not only maintains a~~

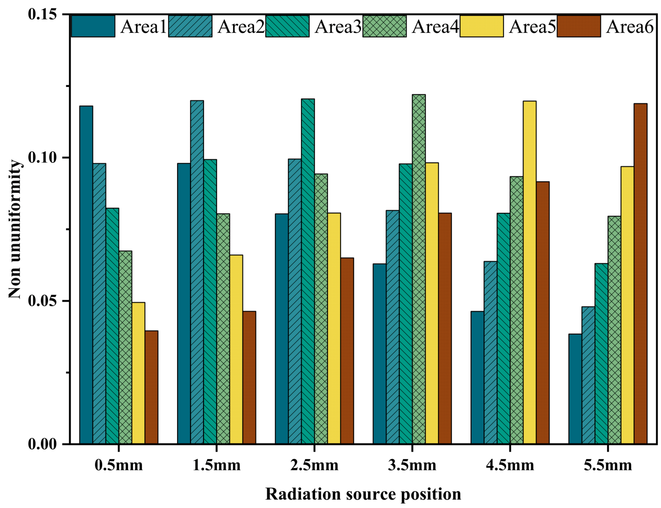

Fig. 10: Accumulated pixel values of the corresponding regions at different irradiation positions

~~high degree of response uniformity but also exhibits high sensitivity and spatial resolution to changes in the radiation source position.~~

Figure 10 demonstrates the nonuniformity distribution across six regions of the CMOS sensor when the radiation source moves in 1.000 mm increments under collimation constraints. As shown, the nonuniformity peak exhibits systematic spatial migration corresponding precisely to the source position. When the collimated source is positioned at the left edge (0.500 mm, Region 1 center), the maximum nonuniformity $R_{\text{nud}} = 0.118$ is observed in Region 1. As the source shifts to 1.500 mm (Region 2 center), the peak migrates to Region 2 ($R_{\text{nud}} = 0.120$), persisting until reaching Region 6 ($R_{\text{nud}} = 0.119$) at 5.500 mm. All regional peaks remain below the 0.125 threshold, with maximum inter-peak variation <2.500%, confirming global response consistency.

With the source fixed at a specific location, nonuniformity displays marked spatial attenuation. Taking the 0.500 mm position (Region 1 center) as an example, nonuniformity decreases progressively from the irradiation core (Region 1: 0.118) to distal regions (Region 6: 0.0396). The attenuation rates between adjacent regions measure 16.800% (Region 1-2), 15.900% (Region 2-3), 18.200% (Region 3-4), 26.600% (Region 4-5), and 19.900% (Region 5-6). Accelerated attenuation in distal regions (4-6) arises from medium absorption reducing particle energy and collimation-induced geometric divergence diminishing particle flux density.

When relocating the radiation source, nonuniformity differences at equivalent normalized distances (Δ) show systematic convergence. For $\Delta = 1$: Nonuniformity measures 0.0993 in Region 3 with the source at 1.500 mm (Region 2), decreasing to 0.0943 in Region 4 when the source moves to 2.500 mm (Region 3) – a 5.100% reduction attributed to collimator-induced flux redistribution. At $\Delta = 2$, the disparity diminishes to 0.300% (Region 4: 0.0804 vs Region 5: 0.0806), caused by drastically reduced particle flux due to cumulative scattering/absorption and weakened contributions from low-energy residual particles. Experimental data confirm inter-regional nonuniformity differences converge below 3.000% when $\Delta \geq 2$. Notably, with the source at the array edge (5.500 mm, Region 6 center), the $\Delta = 1$ region (Region 5) exhibits 0.0969 nonuniformity – merely 2.500% deviation from central regions under equivalent Δ conditions (e.g., Region 3 at 1.500 mm: 0.0993). This validates the system's spatial translation invariance and positioning sensitivity, establishing foundations for radiation source localization.

III. RADIATION SOURCE DISPLACEMENT MEASUREMENT METHOD

A. Measurement Method Based on Distribution Characteristics

Figure 11 shows the algorithm logic flowchart for source displacement judgment. As shown in the figure, a certain number of color images are first converted into dark images. After binarization of the dark images, morphological operations are performed to eliminate noise and obtain clean signal areas. Then, a connected component algorithm is used to identify the response signals in the image, and a curtain with the same size as the image is created to extract the response signals from frame i to frame $i + k$ and superimpose them to construct a point set. The centroid coordinates are calculated as: $\cancel{(x, y) = \left(\frac{1}{n}\sum_{i=1}^{n} x_i, \frac{1}{n}\sum_{i=1}^{n} y_i\right)}$

$$(x, y) = \left(\frac{1}{n}\sum_{i=1}^{n} x_i, \frac{1}{n}\sum_{i=1}^{n} y_i\right) \tag{20}$$

The average distance d from the boundary to the centroid is determined, and circular regions with radii of $0.8d$, $0.6d$, $0.4d$, and $0.2d$ are divided. The signal concentration C in each annular region is calculated as:

$\cancel{C = N_S}$

$$C = \frac{N}{S} \tag{21}$$

where N is the number of response signals in the annular region and S is the area of the region. After processing all the images, the information (radius R, number of response signals N) of the annular region with the highest signal density is summarized. The average value of the radius R and the average number of response signals N are then calculated, and N_{mean} and R_{mean} are output.

DBSCAN algorithm is used to cluster the point set with R_{mean} as the optimal clustering radius and N_{mean} as the minimum sample size. The clusters and outliers are analyzed based on the geometric centroid position, and the entropy weight method is used to calculate the weight of each point. The entropy weight method first calculates the linear distance weight $w_l(p)$ and the density weight matrix $w_d(p)$ as: $\cancel{w_l(p) = \max\left(0, 1 - \frac{\text{dist}(p,\text{centroid})}{R}\right)}$

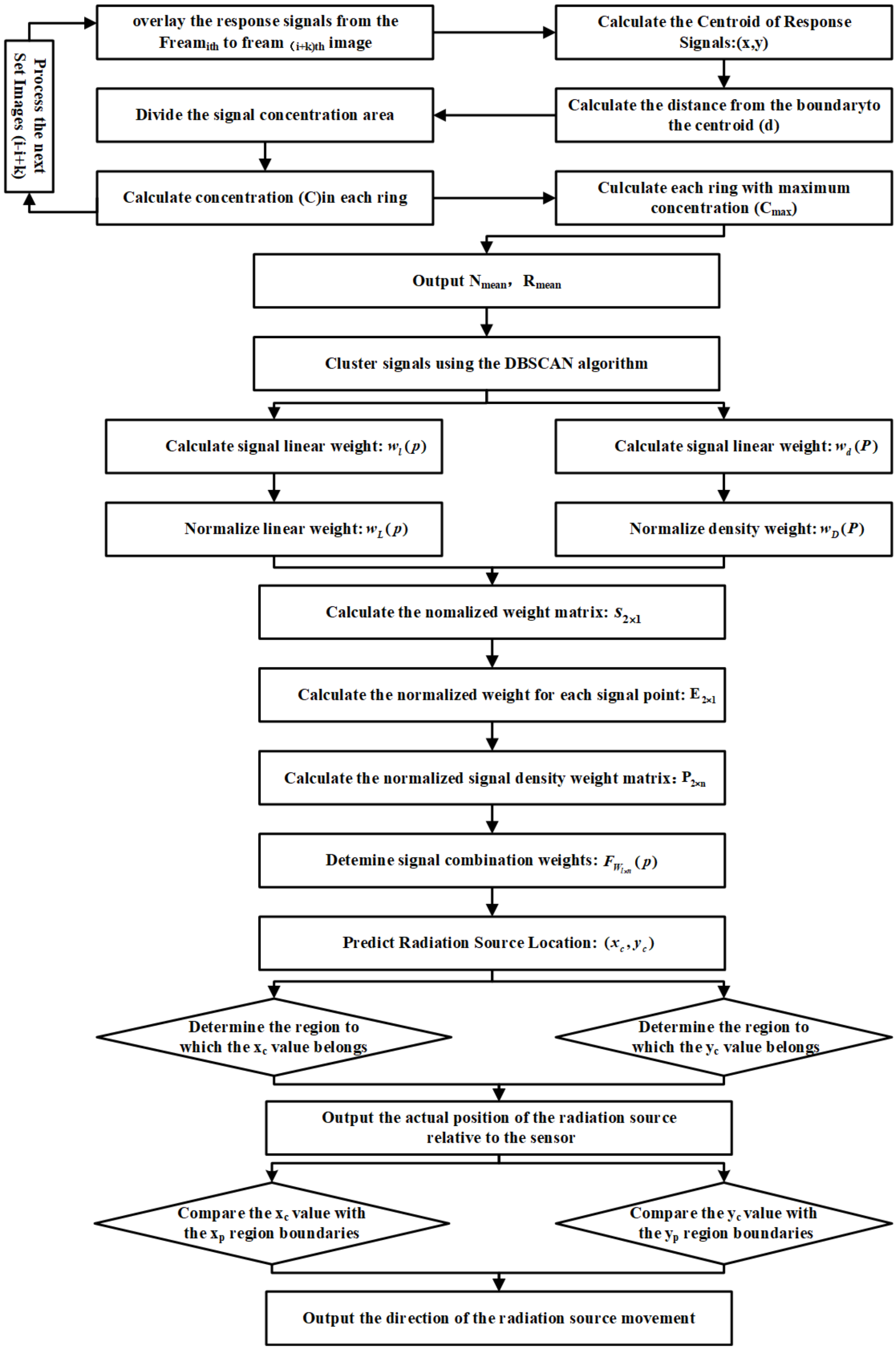

Fig. 11: Algorithm Flowchart

$$w_l(p) = \max\left(0, 1 - \frac{\text{dist}(p, \text{centroid})}{R}\right) \tag{22}$$

where $w_l(p)$ is the position weight of the signal point p, $\text{dist}(p, \text{centroid})$ is the Euclidean distance from the signal point p to the cluster centroid, and R is the average distance from all boundary points to the cluster centroid. The density weight $w_d(p)$ is defined as:

$$w_d(p) = \begin{cases} 5, & \text{if count}(p) \geq \text{density}_t \\ 0.5, & \text{otherwise} \end{cases} \tag{23}$$

where density_t is a density threshold. Next, the linear weight and density weight are normalized as: ~~$w_r(p) = \frac{w_l(p) - w_{l\min}}{w_{l\max} - w_{l\min}}$ $w_L(p) = \frac{w_l(p) - w_{l\min}}{w_r(p)}$~~

$$w_r(p) = \frac{w_l(p) - w_{l\min}}{w_{l\max} - w_{l\min}} \tag{24}$$

$$w_L(p) = \frac{w_l(p) - w_{l\min}}{w_r(p)} \tag{25}$$

where $w_r(p)$ is the range of linear weight, $w_{l\max}$ and $w_{l\min}$ are the maximum and minimum values of the linear weight, and $w_L(p)$ is the normalized linear weight of each point. The density weight is similarly normalized.

After normalization, the entropy weight method is used to determine the combined weight, the normalized weight matrix $S_{2\times 1}$, and the normalized proportion $P_{2\times n}$ of each signal point as: ~~$S_{2\times 1} = \sum T_{2\times n}$, axis = 1 $P_{2\times n} = \frac{T_{2\times n}}{S_{2\times 1}}$~~

$$S_{2\times 1} = \sum T_{2\times n}, \text{axis} = 1 \tag{26}$$

$$P_{2\times n} = \frac{T_{2\times n}}{S_{2\times 1}} \tag{27}$$

where $S_{2\times 1}$ represents the sum of each weight, and $P_{2\times n}$ represents the normalized proportion of each signal point. The entropy value for the linear and density weights is then calculated: ~~$K = 1 \frac{}{\log(n)}$~~ ~~$E_{2\times 1} = -K \cdot \sum P_i \cdot \log(P_{2\times n} + 1e^{-10})$~~

$$K = \frac{1}{\log(n)} \tag{28}$$

$$E_{2\times 1} = -K \cdot \sum P_i \cdot \log(P_{2\times n} + 1e^{-10}) \tag{29}$$

where P_i is the normalized proportion of each index and n is the number of signals. The entropy weight is then calculated from the entropy value:
~~$F_W(p) = E_L \cdot W_L(p) + E_D \cdot W_D(p)$~~

$$F_W(p) = E_L \cdot W_L(p) + E_D \cdot W_D(p) \tag{30}$$

where E_L is the entropy value of the linear weight, $W_L(p)$ is the linear weight, E_D is the entropy value of the density weight, and $W_D(p)$ is the density weight.

Finally, the weighted centroid positions (x_c, y_c) are computed as:
~~$x_c = \frac{\sum_{i=1}^{n} F_i \cdot x_i}{\sum_{i=1}^{n} F_i}, \quad y_c = \frac{\sum_{i=1}^{n} F_i \cdot y_i}{\sum_{i=1}^{n} F_i}$~~

$$x_c = \frac{\sum_{i=1}^{n} F_i \cdot x_i}{\sum_{i=1}^{n} F_i}, \quad y_c = \frac{\sum_{i=1}^{n} F_i \cdot y_i}{\sum_{i=1}^{n} F_i} \tag{31}$$

where x_i, y_i are the coordinates of the i-th signal point and F_i is the final combined weight of the i-th signal point.

By analyzing the predicted centroid coordinates (x_c, y_c) within predefined coordinate regions through their spatial membership relationships, the current radiation source position is determined. The calculated centroid location is then compared with the boundary affiliation of previous centroid coordinates (x_c, y_c) to output the radiation source displacement direction.

B. Algorithm Complexity Analysis

Table 5: Algorithm Module Complexity

Module	Time Complexity	Calculation Basis
Image Processing	$O(N \times M \times K)$	N is the number of images $M \times K$ resolution
Signal Clustering Module	$O(P^2)$	P is the number of detected particle response points
Weighted Centroid Calculation	$O(C \times m^2)$	m is the number of points in a single cluster
Position Determination	$O(1)$	Lookup table within a fixed range
Movement Direction Determination	$O(1)$	Comparison of adjacent centroid region boundaries

The algorithm comprises four primary modules: image preprocessing, signal clustering, weighted centroid calculation, and position determination.The time complexity and computational basis of each module are analyzed in Table 5. Its total time complexity is:

$$T(n) = O(N \times MK) + O(P^2) + O(m^2) + 2 \times O(1) \quad (32)$$

In order to quantify the average time required for the algorithm to generate the predicted results of the radiation source displacement and moving direction under different numbers of superimposed frames, as shown in Fig. 12:

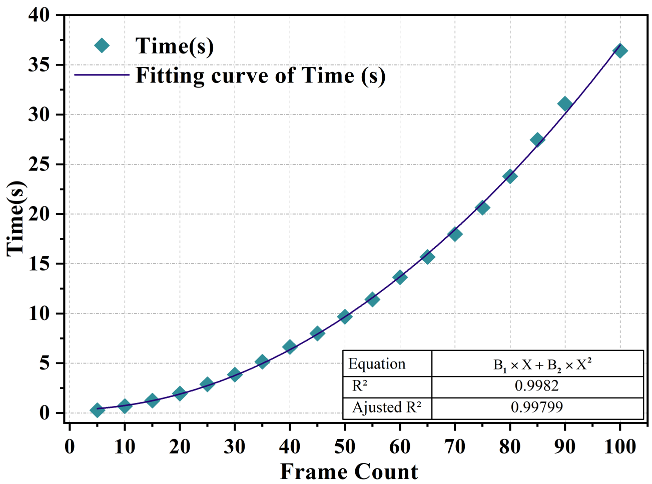

Fig. 12: Algorithm output time under different numbers of superimposed frames

When the number of frames processed in a single group increases from 5 to 100, the result output time increases from 0.35 seconds to 35.72 seconds. For a single group of images with fewer than 15 superimposed frames, the algorithms result output time remains under 1 second.

C. Empirical Experiment on Source Localization

~~Figure 13a presents a comparison of the average distance between the predicted and actual source positions using the traditional centroid method and the weighted centroid method at different numbers of accumulated frames. As shown, the prediction accuracy of both methods improves as the number of frames increases. This improvement occurs because a higher number of frames results in more detected alpha particle events, which reduces random errors and enhances the stability and reliability of the results.~~

~~In the traditional centroid method, when the number of frames is limited, particularly when it is below 20, the deviation between the predicted and actual source positions is large and exhibits significant fluctuations. The initial prediction error typically ranges from 30 to 45 pixels. This substantial error is caused by the radioactive source emitting alpha particles in all directions, combined with the limited number of particle events recorded within a single integration period, leading to an uneven spatial distribution of the signals.Additionally, the traditional centroid method assigns equal weight to all signals, neglecting differences in signal strength and spatial distribution. As a result, outliers, such as occasional pixels with high grayscale values, can have a significant impact on the centroid calculations. As the number of frames increases to 50, the prediction error starts to decrease and eventually stabilizes around 20 pixels. This improvement occurs because the increased number of particle events leads to a more uniform spatial distribution of the signals. Furthermore, as the sample size grows, the influence of outliers on the centroid calculation diminishes. However, the failure of the traditional centroid method to account for variations in signal strength and spatial distribution continues to limit its prediction accuracy.In contrast, the weighted centroid method demonstrates higher accuracy. When fewer than 20 frames are used, the error remains around 20 to 30 pixels; as the number of frames increases to 30, the error decreases further and eventually converges to approximately 8 pixels. This enhanced accuracy arises because the weighted centroid method effectively emphasizes high-intensity signal regions by assigning greater weight to pixels with higher signal strength, thereby biasing the centroid calculation toward the true source location. Additionally, following the inverse square law, the weighted centroid algorithm assigns higher weights to signals closer to the center, further aligning the centroid calculation with the actual source position.~~

~~Figure 13b illustrates the dispersion of predicted source positions using both the weighted centroid and traditional centroid methods, evaluated across varying numbers of accumulated frames. As the number of frames increases, the predictions from both methods progressively converge, leading to enhanced stability in the results. Notably, the weighted centroid method yields more concentrated predictions and converges more rapidly compared to the traditional centroid method.For smaller frame counts, specifically when fewer than five frames are used, both methods exhibit comparable dispersion in the predicted source positions. This is attributed to the limited data points, which result in weak distribution characteristics of the response signals and obscure high-density regions. As the number of frames increases, the weighted centroid method demonstrates a faster convergence. When the frame count exceeds thirty, the average distance between predicted positions using the weighted centroid method stabilizes between 10 and 20 pixels.In contrast, the traditional centroid method maintains a larger average distance of approximately 40 to 60 pixels and shows greater error variability.Furthermore, the traditional centroid method tends to produce more dispersed predictions, particularly when the source is near the boundary of the region, which increases the likelihood of misjudgments. Once the number of frames exceeds fifty, the average distance for the traditional centroid method decreases slightly but stabilizes at a higher value, ranging from 20 to 30 pixels. This final value remains significantly greater than the convergence value observed for the weighted centroid method, highlighting the latters superior accuracy and stability in source position prediction.~~

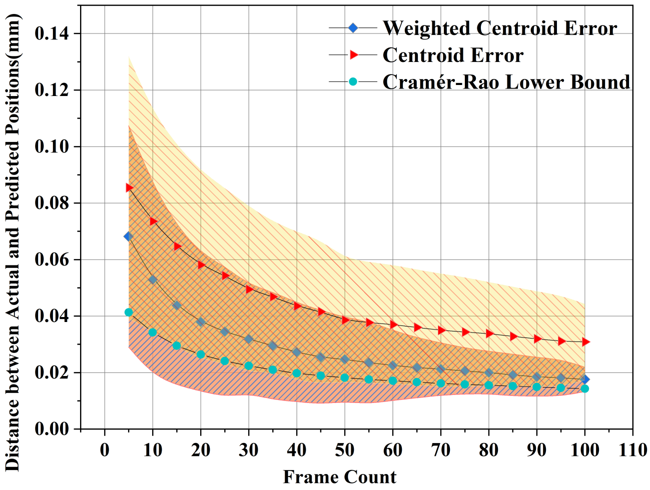

(a) Distance between the predicted and actual positions

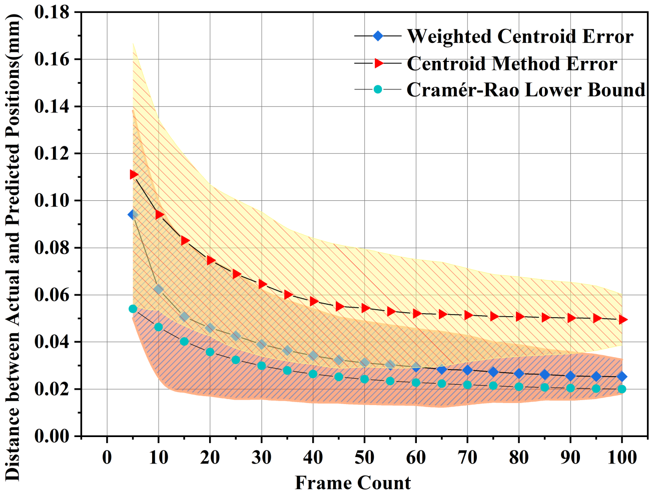

(b) Distance between predicted positions when the radiation source at the same location

Fig. 13: Accuracy analysis of the centroid method

Figure 13a illustrates the comparison of the average distance between the predicted source location and the actual location for both the traditional centroid method and the weighted centroid method under different accumulated frame counts. As shown in the figure, with the increase in the number of frames, the prediction accuracy of both methods gradually improves. When the number of accumulated frames increases from 5 to 100, the average prediction error of the weighted centroid method decreases from 0.0718 mm±0.0032 mm to 0.0176 mm±0.0008 mm, while the traditional centroid method converges from 0.0855 mm±0.0051 mm to 0.0309 mm±0.0015 mm. During this process, the accuracy improvement rate of the weighted centroid method increases from an initial 18.98% to 42.97%. Compared with the theoretical accuracy limit of this method, its error margin narrows from 1.732 to 1.35.

In the low-frame-count stage (5–25 frames), the traditional centroid method exhibits a larger prediction error and a slower convergence speed, ranging between 0.0855 mm and 0.0543 mm, with a 36.49% accuracy improvement. This is primarily due to the limited number of particle events under fewer frames. Meanwhile, the conventional approach of treating all signals with equal weight overlooks differences in signal intensity and spatial distribution, causing outlier signal positions to significantly interfere with the centroid calculation when the signal count is low. As the frame count increases to 65 frames, the prediction error begins to converge down to 0.0309 mm. This convergence is attributed to the signal spatial distribution being balanced by the accumulated particle events and the dilution effect of large sample sizes on outliers. However, the insensitivity of the traditional method to the signal intensity gradient still restricts further accuracy improvement.

By contrast, the weighted centroid method achieves smaller errors and faster convergence in the low-frame-count stage (5–25 frames), with errors ranging from 0.07182 mm to 0.0375 mm, representing a 47.78% accuracy improvement. When the number of superimposed frames reaches 45, the error converges rapidly to 0.0176 mm. This is because the density-weighting mechanism highlights regions of high-density signals, shifting the centroid calculation toward the true source position. In addition, the weight allocation based on the inverse-square law enhances the contribution of nearby signals, thereby further improving localization accuracy.

To analyze the dispersion of the predicted locations obtained by the two methods, Figure 13b shows the average distance between each predicted location for the two methods. As shown in the figure, with the increase in the number of frames, the prediction results of both methods gradually converge, and the stability is significantly improved. When the number of accumulated frames increases from 5 to 100, the average distance of the predicted locations using the weighted centroid method decreases from 0.0941 mm to 0.0253 mm, while that of the traditional centroid method decreases from 0.1111 mm to 0.0495 mm, a reduction of 55.45%. The difference between the two groups expands from an initial 15.23% to a final 48.89%. Notably, in the range of 25–45 superimposed frames, the average distance of the weighted centroid method converges rapidly at a rate of 0.0102 mm per 10 frames, which is a 35.94% improvement over the 0.0138 mm per 10 frames rate of the traditional centroid method. Therefore, compared with the traditional method, the predicted locations obtained by the weighted centroid method are more clustered, thereby reducing the risk of misjudging displacements.

~~Figure 14 illustrates the maximum, minimum, and average distances between adjacent irradiation positions (spaced 1 millimeter apart) as predicted by the weighted centroid method under varying numbers of accumulated frames. As shown in the figure, with an increasing number of frames, both the maximum and minimum distances between adjacent predicted irradiation positions gradually converge toward the average predicted distance. Specifically, the maximum predicted distance decreases from 560 pixels to approximately 460 pixels, while the minimum distance increases from 300 pixels to about 420~~

~~pixels. The average distance is around 440 pixels, with an error of approximately 8 pixels compared to the actual irradiation positions.Additionally, the range of predicted distance variations progressively narrows, indicating that as the number of accumulated frames increases, the error between predicted and actual positions decreases, and prediction accuracy improves. The distribution range of the radioactive source's predicted positions also becomes narrower, converging from an initial spread of 260 pixels to 40 pixels. This improvement is attributed to the accumulation of frames, which clarifies the signal distribution characteristics and allows for a more rational allocation of signal weights, thereby reducing the distance between predicted and actual positions.~~

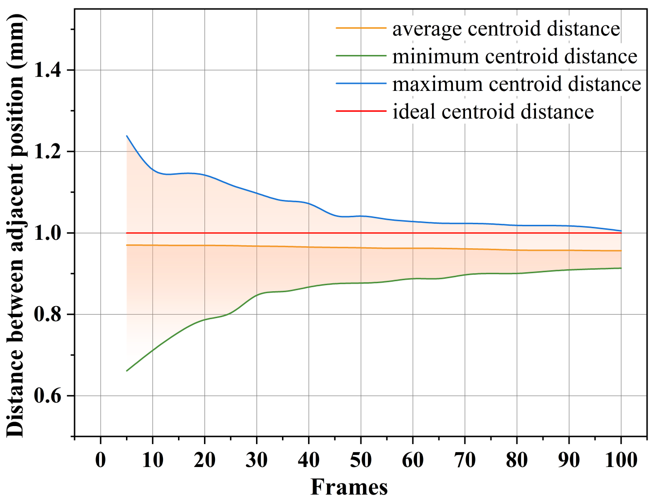

Fig. 14: Centroid Distances Between Adjacent Positions

Figure 14 presents the maximum, minimum, and average distances of adjacent irradiation positions (separated by 1 mm) predicted by the weighted centroid method under different accumulated frame counts. As shown in the figure, with the increase in the number of frames, the maximum and minimum distances of adjacent predicted irradiation positions gradually converge toward the average predicted distance, and the error between the average predicted spacing of adjacent radiation sources and the actual spacing also decreases. The absolute error declines from an initial 0.0435 mm to 0.0298 mm, and the relative error decreases from 4.35% to 2.98%. This improvement is attributed to the enhanced clarity of signal distribution characteristics via frame accumulation. By assigning more appropriate weights to the signals, the distance error between the predicted and actual source locations is effectively reduced.

D. Empirical Experiment on Source Displacement Direction Prediction and Measurement

~~Figure 15 shows the displacement and measurement verification results of the radioactive source moving in two different directions using the weighted centroid algorithm.In Figure 15a, the radioactive source moves along the horizontal (X-axis) direction. The linear regression results indicate that the predicted path closely aligns with the actual movement path, with a regression slope of −0.0117. The angle error between the predicted and actual trajectories is −0.68°, demonstrating minimal position change along the Y-axis (vertical direction) during horizontal movement. This confirms that the algorithm can accurately capture the lateral displacement of the radioactive source. Figure 15b illustrates the movement of the radioactive source along the vertical (Y-axis) direction. The regression slope is 12.6782, and the angle error between the predicted and actual trajectories is 1.53°, indicating a high degree of alignment between the predicted and actual paths.~~

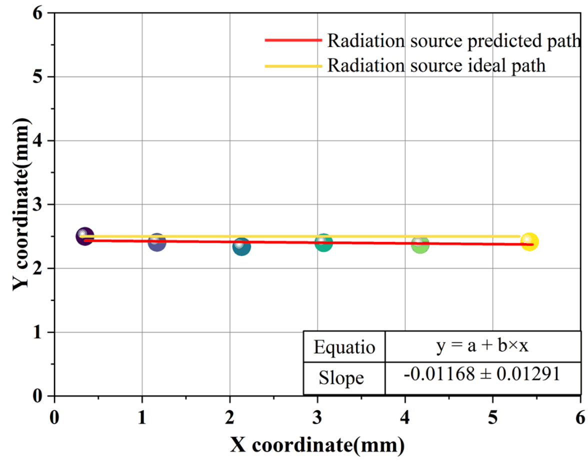

(a) Fitting of Horizontal Movement Path

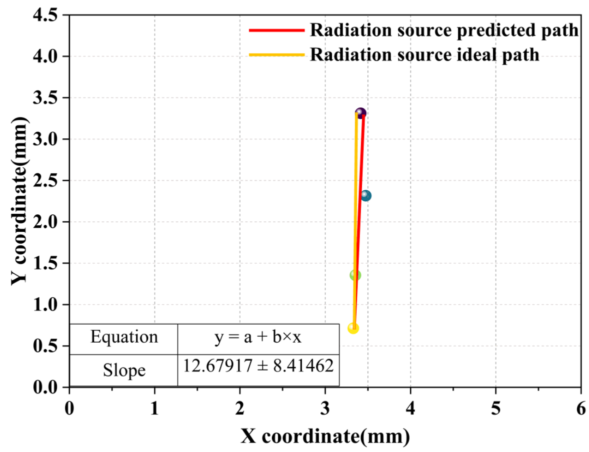

(b) Fitting of Vertical Movement Path

Fig. 15: Trajectory Fitting of the Movement Paths

Figure 15 shows the displacement measurement verification results based on the weighted centroid algorithm for a radioactive source moving in two different directions. Figure 15a depicts the source moving horizontally (along the X-axis), where the red solid line represents the linear regression line of the sources position, and the yellow solid line represents the ideal path of the source with a slope of 0. The

linear regression results indicate a high degree of agreement between the predicted motion path and the actual path, with a regression slope of 0.0117. The angle error between the predicted trajectory and the actual trajectory is 0.68.

Figure 15b illustrates the radioactive source moving vertically (along the Y-axis). The red solid line denotes the linear regression line of the sources position during longitudinal displacement, and the yellow solid line represents the ideal path. The regression slope is 12.6782, and the linearity of the vertical motion path is 88.47. The angle error between the predicted trajectory and the actual trajectory is 1.53, which again demonstrates a high level of consistency between the predicted path and the actual motion trajectory.

~~Figure 16 illustrates the variation in centroid coordinates, as determined by the weighted algorithm, during the uniform horizontal and vertical movements of the radioactive source. In the horizontal movement (Figure 16a), the slope is 421.3328, corresponding to an error of 11.67 pixels in displacement rate. In the vertical movement (Figure 16b), the slope is -465.21, with an error of 20.79 pixels. In both directions, the algorithm predicts the displacement rate of the weighted centroid with an error of less than 5% compared to the actual displacement rate of the radioactive source.~~

Figure 16 presents the variation in the weighted centroid coordinates when the radioactive source moves at a constant speed horizontally and vertically. Among them, Figure 16a shows the change in the centroid coordinates of the source during uniform horizontal motion. The yellow coordinates indicate the ideal X-coordinate of the source, with a speed of 1.00 mm/s, and the red coordinate points represent the current predicted X-coordinate of the source by the algorithm. After fitting, the predicted displacement speed of the source in horizontal motion is 1.03±0.08 mm/s. Figure 16b illustrates the actual and predicted Y-coordinates of the source when it moves vertically. The yellow coordinates represent the ideal Y-coordinate of the source, which has a speed of 1.00 mm/s, and the green coordinates indicate the current predicted Y-coordinate by the algorithm. After fitting, the predicted displacement speed of the source is -0.97±0.06 mm/s. The speed error in both cases is less than 5%.

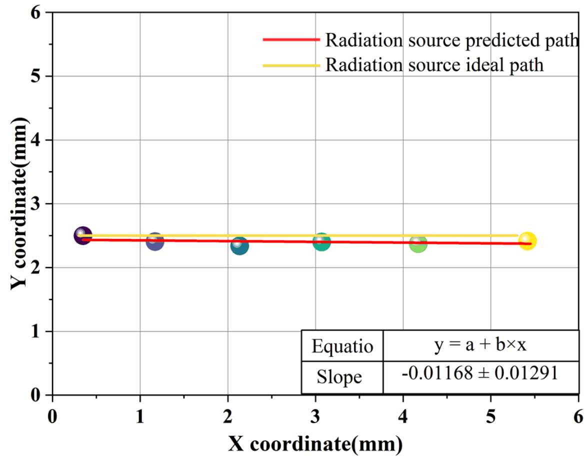

(a) Fitting of Horizontal Movement (X-Coordinate) with Time

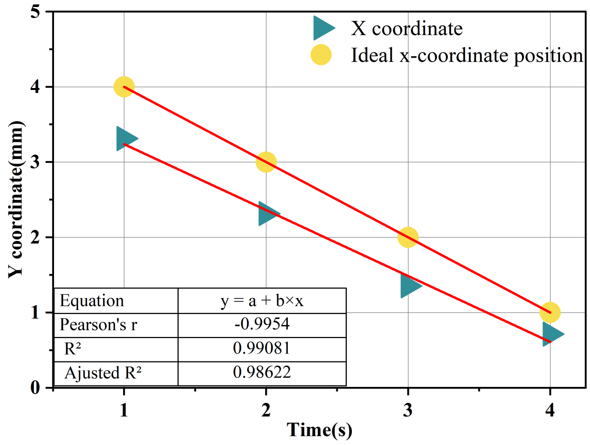

(b) Fitting of Vertical Movement (Y-Coordinate) with Time

Fig. 16: Fitting of Coordinates with Time

IV. DISCUSSION

Based on the morphological features of radiation response events and the distribution characteristics of response signals under the influence of the collimator structure, this paper introduces the DBSCAN density clustering algorithm and proposes a localization method for static α radiation sources. Experimental results verify that its localization accuracy for static radiation sources ranges from 0.072 mm to 0.018 mm, whereas the accuracy range of similar localization techniques spans 0.1 mm to 0.01 mm[45, 46]. Compared with similar techniques, this method achieves comparable accuracy but offers higher localization precision and faster response under lower frame counts, while also having a smaller device size and lower cost. Based on our experimental findings, micron-level detection accuracy can be attained. This technique can be applied to in-situ deformation detection of high-precision instruments on a sub-millimeter scale by affixing an α radiation source onto the surface of a high-precision instrument (e.g., bearings, gears, lithium batteries) and monitoring it in real time using an external CMOS sensor. When the instrument undergoes deformation, the resultant change in the source position enables the measurement or early warning of micro-deformation, thereby replacing traditional contact-based strain gauges. Furthermore, owing to its high sensitivity for detecting α radiation sources under low-frame-count conditions (where the response time is less than 1 s for fewer than 15 superimposed frames), this technique can be developed into a non-contact surface contamination detector. By constructing a radioactive contamination area distribution map based on the relative displacement trajectory between the detector and the radiation source, the detection efficiency for surface contamination can be significantly improved while reducing costs.

V. CONCLUSION

~~This paper presents a method for localizing and measuring the displacement of radioactive sources using CMOS active pixel sensors. By analyzing the response characteristics of active pixel sensors under varying α radiation irradiation conditions, we investigated the distribution patterns of response signals under collimator structure interference. Based on this analysis, we developed a displacement judgment and measurement method utilizing the weighted centroid algorithm, followed by experimental validation. The results demonstrate that:~~

~~The gray values of α particle response signals are predominantly concentrated between 150 and 255, typically comprising 3 to 8 high-gray-value pixels. These pixels exhibit a highly concentrated distribution pattern and respond uniformly across the entire pixel array. Regarding the distance between adjacent predicted positions, the maximum predicted distance decreases from 560 pixels to approximately 460 pixels, while the minimum distance increases from 300 pixels to about 420 pixels. The average distance is around 440 pixels, with an error of approximately 8 pixels compared to the actual irradiation positions.~~

~~When tracking a continuously moving radioactive source under low frame conditions, the predicted path closely aligns with the actual path. The angle of the predicted horizontal movement path is 0.01ř, and the linearity of the vertical movement path is 88.47ř. The angle error between the predicted and actual paths is less than 1.53%. Additionally, in both displacement modes, the predicted centroid displacement rate exhibits a small error relative to the actual displacement rate of the radioactive source, with errors below 5% of the actual movement speed. Specifically, the predicted horizontal movement speed is 421.3328 pixels, with an error of 11.6672 pixels compared to the actual displacement speed. The predicted vertical movement speed is -465.2105 pixels, with an error of 20.7895 pixels compared to the actual vertical speed. These results further validate the reliability and accuracy of the proposed method for judging radioactive source displacement.~~

~~CMOS sensors offer excellent spatial resolution and uniform response characteristics. Utilizing the weighted centroid algorithm, the position of the radioactive source can be effectively predicted, and its movement direction and path can be accurately identified, demonstrating significant potential for future applications.~~

This paper proposes a method using a CMOS active pixel sensor for locating and measuring the displacement of a radiation source. By analyzing the response characteristics of the active pixel sensor under different α radiation conditions, we investigated the distribution pattern of response signals when interfered by the collimator structure. Based on this analysis, we developed a radiation source localization and displacement direction determination method using a weighted centroid algorithm and conducted experimental validation. The results show:

The gray values of α particle response signals primarily range from 150 to 255, typically consisting of 3 to 8 high-gray-value pixels. These pixels exhibit a highly concentrated distribution pattern. When the sensor is irradiated by the radiation source, the irradiated area shows a consistent response trend and demonstrates high sensitivity and spatial resolution to changes in the radiation source position.

Using the weighted centroid algorithm for static radiation source localization, the error converges from 0.07182 mm to 0.0375 mm. Compared with the theoretical accuracy limit of this method, the error margin narrows from 1.732 to 1.35, achieving sub-millimeter-level localization accuracy. For adjacent predicted positions spaced 1 mm apart, the absolute error decreases from an initial 0.0435 mm to 0.0298 mm, while the relative error declines from 4.35% to 2.98%.

Under low frame-rate conditions for tracking a continuously moving radiation source, the predicted path aligns closely with the actual path. The angle error between the horizontal predicted trajectory and the actual trajectory is 0.68, and the linearity of the vertical motion path is 88.47, with the angle error between the predicted and actual trajectories being 1.53. Furthermore, in both displacement modes, the error between the predicted centroid displacement rate and the actual displacement speed of the radiation source is less than 5%, confirming the reliability and accuracy of the proposed radiation source displacement determination method.

[1] J.H. Lee, J.I. Byun, D.M. Lee, et al., In-situ $CeBr_3$ gamma-ray spectrometry for radioactivity analysis of soil. *Journal of Radioanalytical and Nuclear Chemistry*, vol. 321, no. 2 (2019). DOI: 10.1007/s10967-019-06621-7

[2] F.H. Ruddy, J.G. Seidel, H. Chen, et al., High-resolution alpha-particle spectrometry using 4H silicon carbide semiconductor detectors. *IEEE Transactions on Nuclear Science*, vol. 53, no. 5, pp. 2983-2987 (2006). DOI: 10.1109/TNS.2006.880706

[3] J. Smith, A. Johnson, GammaRay Detection Efficiency and Image Resolution in Sodium Iodide. *Review of Scientific Instruments*, vol. 35, no. 6, pp. 693-698 (1964). DOI: 10.1063/1.1712294

[4] J. Dumazert, R. Coulon, Q. Lecomte, et al., Gadolinium for neutron detection in current nuclear instrumentation research: A review. *Nuclear Instruments and Methods in Physics Research Section A*, vol. 882, pp. 53-68 (2018). DOI: 10.1016/j.nima.2017.11.032

[5] Y.N. Zhang, Q. Liu, H.B. Liu, et al., Study of a sealed high gas pressure THGEM detector and response of alpha particle spectra. *Chinese Physics C*, vol. 41, no. 4 (2017). DOI: 10.1088/1674-1137/41/4/046001

[6] N. Hasebe, M. Miyajima, E. Shibamura, et al., α-particle spectrometer based on xenon gas ionization chamber using coplanar electrodes. *Nuclear Instruments and Methods in Physics Research Section A*, vol. 925, pp. 123–127 (2019). DOI: 10.1016/j.nima.2019.01.079

[7] Q. Du, S.T. Lin, H.T. He, et al., Response of gadolinium doped liquid scintillator to charged particles: measurement based on

intrinsic U/Th contamination. *Journal of Instrumentation*, vol. 13, no. 04 (2018). DOI: 10.1088/1748-0221/13/04/P04001

[8] K. Yasuda, S. Usuda, H. Gunji, et al., Properties of a YAP powder scintillator as alpha-ray detector. *Applied Radiation and Isotopes*, vol. 52, no. 03 (2000). DOI: 10.1016/S0969-8043(99)00179-7

[9] N. Stevanovic, V.M. Markovicx, M. Milosevicx, et al., Correlations between track parameters in a solid-state nuclear track detector and its diffraction pattern. *Radiation Physics and Chemistry* (2022). DOI: 10.1016/j.radphyschem.2022.1099862

[10] T.L. Cardoso, S.T. Oliveira, R.M. Marques Pinheiro, et al., Radon dosimetry using Solid State Nuclear Track Detectors in different environments: a review. *Applied Radiation and Isotopes*, vol. 186 (2022). DOI: 10.1016/j.apradiso.2022.110217

[11] A. Gola, K. Majumdar, G. Casse, et al., First Demonstration of the Use of LG-SiPMs for Optical Readout of a TPC. *Journal of Instrumentation*, vol. 15, no. 12 (2020). DOI: 10.1088/1748-0221/15/12/P12017

[12] Y. Li, H. Yi, Y.K. Sun, et al., Performance study of the Multi-purpose Time Projection Chamber (MTPC) using a four-component alpha source. *Nuclear Instruments and Methods in Physics Research*, vol. 1060 (2024). DOI: 10.1016/j.nima.2023.169045

[13] M. Cortesi, J. Pereira, D. Bazin, et al., Development of a novel MPGD-based drift chamber for the NSCL/FRIB S800 spectrometer. *Journal of Instrumentation*, vol. 15, no. 03, pp. 3–25 (2020). DOI: 10.1088/1748-0221/15/03/P03025

[14] Z.W. Qin, S.L. Xu, H.F. Dong, et al., Research on Calculation Method of Radiation Response Eigenvalue of a Single-Chip Active Pixel Sensor. *Sensors*, vol. 22, no. 13 (2023). DOI: 10.3390/s22134815

[15] D.V. Gorbachev, V.I. Ivanov, S.Yu. Tikhonov, et al., High resolution detection of fast particles with the Timepix3 hybrid pixel detector. arXiv, (2019). DOI: 10.48550/arXiv.1912.03743

[16] Y. Jin, P. Cristaudo, A. Gabrielli, et al., Simulation of the response of a diamond-based radiation detector to ultra-short and intense high-energy electron pulses. *Nuclear Instruments and Methods in Physics Research Section A: Accelerators, Spectrometers, Detectors and Associated Equipment*, vol. 1052, p. 168259 (2023). DOI: 10.1016/j.nima.2023.168259

[17] Y. Dieter, M. Daas, J. Dingfelder, et al., Radiation tolerant, thin, passive CMOS sensors read out with the RD53A chip. *Nuclear Instruments and Methods in Physics Research Section A: Accelerators, Spectrometers, Detectors and Associated Equipment*, vol. 1015, p. 165771 (2021). DOI: 10.1016/j.nima.2021.165771

[18] L.M. Carvalho Freitas, F. Morgado-Dias, Thermal readout noise comparison of classical constant bias APS and switching bias APS used in CMOS image sensors. *Analog Integrated Circuits and Signal Processing* (2022). DOI: 10.1007/s10470-021-01964-2

[19] S.L. Xu, S.L. Zou, Y.C. Han, et al., Obtaining High-Dose-Rate γ-Ray Detection With Commercial Off-the-Shelf CMOS Pixel Sensor Module. *IEEE Sensors Journal*, vol. 19, no. 16, pp. 6729–6735 (2019). DOI: 10.1109/JSEN.2019.2912198

[20] H. Deng, H. Zhang, H. Zhao, et al., γ radiation image denoising method based on speckle splitting. *Signal, Lecture Notes in Computer Science*, vol. 17, no. 4, pp. 1391–1399 (2023). DOI: 10.1007/s11760-022-02347-4

[21] J. Feng, J. Fu, Y.D. Li, et al., Mechanism of Ionization Damage in Large Eight-Transistor Complementary MetalOxideSemiconductor Color Image Sensors. *Journal of Nanoelectronics and Optoelectronics*, vol. 16, no. 11, pp. 1755–1761 (2021). DOI: 10.1166/jno.2021.3136

[22] S. Haro, M. Bessia, F. Perez, et al., Soft X-rays spectroscopy with a commercial CMOS image sensor at room temperature. *Radiation Physics and Chemistry*, vol. 167 (2020). DOI: 10.1016/j.radphyschem.2019.108354

[23] R.P. Alikunju, S. Kearney, R. Moss, et al., Effect of different scintillator choices on the X-ray imaging performance of CMOS sensors. *Nuclear Instruments and Methods in Physics Research Section A*, vol. 1050 (2023). DOI: 10.1016/j.nima.2023.168136

[24] S. Staeck, Y. Kayser, J. Baumann, et al., Towards soft x-ray fluorescence measurements in the laboratory using a laser-produced plasma source and a complementary metal-oxide semiconductor detector. *Journal of Instrumentation*, vol. 16, no. 03 (2021). DOI: 10.1088/1748-0221/16/03/P03033

[25] J. Teng, L.Q. Shan, B. Zhu, et al., A compact online proton spectrometer for diagnosis of picosecond intense-laser accelerated protons. *AIP Advances*, vol. 13, no. 11 (2023). DOI: 10.1063/5.0171418

[26] X. Zha, M.M. El-Gomati, L. Chen, et al., Direct detection of low-energy electrons with a novel CMOS APS sensor. *IEEE Transactions on Electron Devices*, vol. 59, no. 12, pp. 3594–3600 (2012). DOI: 10.1109/TED.2012.2219623

[27] S.L. Xu, S.L. Zou, Y.C. Han, et al., Ionizing radiation response uniformity of solid-state image sensors. *Acta Optica Sinica*, vol. 39, pp. 1-6 (2019). DOI: 10.3788/AOS201939.0728007

[28] S.L. Xu, J. Velthuis, Q.F. Wu, et al., Effect of commercial off-the-shelf MAPS on -ray ionizing radiation response. *Sensors*, vol. 19, p. 4950 (2019). DOI: 10.3390/s19224950

[29] Q. Zhao, Z. Liu, J. Wang, et al., Random Telegraph Noises in CMOS Image Sensors Caused by Variable Gate-Induced Sense Node Leakage Due to X-Ray Irradiation. *IEEE Transactions on Nuclear Science*, vol. 66, pp. 1129-1135 (2019). DOI: 10.1109/JEDS.2019.2893299

[30] C.Q. Wu, et al., Network Detection of Radiation Sources Using Localization-Based Approaches. *IEEE Transactions on Industrial Informatics*, vol. 15, no. 4, pp. 2308-2320 (2019). DOI: 10.1109/TII.2019.2891253

[31] V. Astromskas, et al., Real-time source localisation by passive, fast-neutron time-of-flight with organic scintillators for facility-installed applications. *Nuclear Instruments and Methods in Physics Research Section A: Accelerators, Spectrometers, Detectors and Associated Equipment*, vol. 994, p. 65094 (2021). DOI: 10.1016/j.nima.2021.165094

[32] F. Mascarich, T. Wilson, C. Papachristos, et al., Radiation Source Localization in GPS-Denied Environments Using Aerial Robots. In *2018 IEEE International Conference on Robotics and Automation (ICRA)*, Brisbane, QLD, Australia, 2018, pp. 6537-6544. DOI: 10.1109/ICRA.2018.8460760

[33] Y. Kong, et al., A Prototype Compton Camera Array for Localization and Identification of Remote Radiation Sources. *IEEE Transactions on Nuclear Science*, vol. 60, no. 2, pp. 1066-1071 (2013). DOI: 10.1109/TNS.2012.2222665

[34] A. Molnár, D. Kiss, Z. Domozi, et al., Radiation Source Localization Using a Model-Based Approach. *Sensors*, vol. 23, p. 5983 (2023). DOI: 10.3390/s23135983

[35] W. Lu, H.W. Zhang, M.Z. Liu, et al., Generalization ability of a CNN -ray localization model for radiation imaging. *Nuclear Science and Technology*, vol. 34, p. 185 (2023). DOI: 10.1007/s41365-023-01323-y

[36] R. Okabe, S. Xue, J.R. Vavrek, et al., Tetris-inspired detector with neural network for radiation mapping. *Nature Communications*, vol. 15, p. 3061 (2024). DOI: 10.1038/s41467-024-

47338-w
[37] D. Woller, M. Kulich, Path planning algorithm ensuring accurate localization of radiation sources. *Applied Intelligence*, vol. 52, pp. 95749596 (2022). DOI: 10.1007/s10489-021-02941-y
[38] W. Lu, L. Wang, Y. Yuan, et al., Monte Carlo simulation for performance evaluation of detector model with a monolithic $LaBr_3$(Ce) crystal and SiPM array for radiation imaging. *Nuclear Science and Technology*, vol. 33, p. 107 (2022). DOI: 10.1007/s41365-022-01081-3
[39] H.H. Chen-Mayer, D. Sahin, B. Remley, et al., Calibration of a gamma ray Compton camera for radioactivity measurements. *Journal of Radioanalytical and Nuclear Chemistry*, vol. 333, pp. 66456651 (2024). DOI: 10.1007/s10967-024-09729-7
[40] M. Ester, H. P. Kriegel, J. Sander, et al., A density-based algorithm for discovering clusters in large spatial databases with noise. KDD'96, pp. 226-231 (1996). DOI: 10.5555/3001460.3001497
[41] Z. H. Zhou, Machine Learning. Tsinghua University Press, Beijing, 2021. DOI: 10.4236/jilsa.2017.91001
[42] ON Semiconductor, MT9P031: 1/2-Inch 5 Mp CMOS Digital Image Sensor. Data Sheet Rev. D, 2023. https://www.onsemi.com/download/data-sheet/pdf/mt9p031-d.pdf
[43] I. Djurovi, Achieving CramerRao Lower Bounds in Sensor Network Estimation. *IEEE Sensors Letters*, vol. 2, no. 1, pp. 1-4 (2018). DOI: 10.1109/LSENS.2018.2795699
[44] C. Shi, S. Salous, F. Wang, et al., Cramer-Rao Lower Bound Evaluation for Linear Frequency Modulation Based Active Radar Networks Operating in a Rice Fading Environment. *Sensors*, vol. 16, p. 2072 (2016). DOI: 10.3390/s16122072
[45] K-H. Kim, H-K. Jung, Development of a Remote Displacement Measuring Laser System for Bridge Inspection. *Sensors*, vol. 22, no. 5, p. 1963 (2022). DOI: 10.3390/s22051963
[46] G. Yang, et al., A Novel 0.1 mm 3D Laser Imaging Technology for Pavement Safety Measurement. *Sensors*, vol. 22, p. 8038 (2022). DOI: 10.3390/s22208038